energies

MDPI

Article

Numerical Simulation Method for the Aeroelasticity of Flexible Wind Turbine Blades under Standstill Conditions

Xianyou Wu [1,*], Rongxiang Liu [2], Yan Li [3], Pin Lv [3], Chuanqiang Gao [2] and Kai Feng [1]

[1] College of Mechanical and Vehicle Engineering, Hunan University, Changsha 410082, China; kfeng@hnu.edu.cn
[2] School of Aeronautic, Northwestern Polytechnical University, Xi'an 710072, China; 15734632898@163.com (R.L.); gaocq@nwpu.edu.cn (C.G.)
[3] Beijing Goldwind Science & Creation Windpower Equipment Co., Ltd., Beijing 100176, China; liyan26368@goldwind.com (Y.L.); lvpin@goldwind.com (P.L.)
* Correspondence: wuxianyou@goldwind.com

Abstract: With the trend towards larger and lighter designs of wind turbines, blades are progressively being developed to have longer and more flexible configurations. Under standstill conditions, the separated flow induced by a wide range of incident flow angles can cause complex aerodynamic elastic phenomena on blades. However, classical momentum blade element theory methods show limited applicability at high angles of attack, leading to significant inaccuracies in wind turbine performance prediction. In this paper, the geometrically accurate beam theory and high-fidelity CFD method are combined to establish a bidirectional fluid–structure coupling model, which can be used for the prediction of the aeroelastic response of wind turbine blades and the analysis of fluid–structure coupling. Aeroelastic calculations are carried out for a single blade under different working conditions to analyze the influence of turbulence, gravity and other parameters on the aeroelastic response of the blade. The results show that the dominant frequency of the vibration deformation response in the edgewise direction is always the same as the first-order edgewise frequency of the blade when the incoming flow condition is changed. The loading of gravity will make the aeroelastic destabilization of the blade more significant, which indicates that the influence of gravity should be taken into account in the design of the aeroelasticity of the wind turbine. Increasing the turbulence intensity will change the dominant frequency of the vibration response in the edgewise direction, and at the same time, it will be beneficial to the stabilization of the aeroelasticity response.

Keywords: wind turbine blade; fluid–structure coupling; aeroelastic analysis; edgewise vibration

Citation: Wu, X.; Liu, R.; Li, Y.; Lv, P.; Gao, C.; Feng, K. Numerical Simulation Method for the Aeroelasticity of Flexible Wind Turbine Blades under Standstill Conditions. *Energies* **2024**, *17*, 3395. https://doi.org/10.3390/en17143395

Academic Editor: Davide Astolfi

Received: 12 May 2024
Revised: 19 June 2024
Accepted: 5 July 2024
Published: 10 July 2024

1. Introduction

As wind turbines become larger and lighter in their design, their risk of aeroelastic instability gradually increases, seriously affecting their safety and stability. The standstill condition of wind turbine blades refers to the critical load condition when the turbine yaw or pitch system fails. Under standstill conditions, blades will withstand extreme wind speeds in different directions and have large angles of attack, which can easily cause flow separation and produce complex aeroelastic instability phenomena [1], such as stall flutter [2], vortex-induced vibration [3], bending–torsional coupled flutter [4], etc. Due to the numerous types of aeroelastic instability under this working condition, the coupling response is complex, and the induction mechanism is unclear. It is necessary to develop a high-precision simulation method for wind turbine aeroelasticity to achieve accurate predictions of unsteady and nonlinear dynamic responses. Further in-depth research on the mechanism of complex aeroelastic problems under standstill conditions is needed.

At present, the main methods for analyzing and predicting the aeroelasticity of wind turbines include aeroelastic wind tunnel tests and numerical simulation analysis methods. Aeroelastic wind tunnel testing [5] stands out as a method capable of achieving more

realistic physical simulations. This is particularly relevant given that the length of wind turbine blades has now reached the order of hundreds of meters. There are defects in model scaled-down wind tunnel experiments that cannot be fully satisfied by similar criteria. For example, when geometric similarity is satisfied, there are problems such as excessive model mass and difficulty corresponding to high-order frequencies [6,7]. Traditional FSI prediction methods mainly use simplified engineering coupling algorithms, such as the BEM/finite element method [8], BEM/modal analysis method [9,10] and others. Although the calculation efficiency is high, there are problems with the calculation accuracy. Among them, the BEM method [11] has a high efficiency and accuracy that can be accepted in engineering for load and power calculations under normal working conditions. However, it fails to accurately describe phenomena like stalling caused by large-angle separation flow under standstill conditions, thus limiting its ability to simulate the unsteady and nonlinear flow effects that significantly impact the coupled system.

In recent years, the coupling method of the CFD method that directly solves the Navier–Stokes equation has gradually started to be used in wind turbine simulation calculations. Witold Skrzypiński et al. [12,13] used the fluid–structure coupling simulation method based on the CFD method to conduct a simulation study on the vortex-induced vibration phenomenon of the DU91-W-180 airfoil at a 90-degree angle of attack and compared the differences between two-dimensional and three-dimensional calculations. In 2016, Heinz et al. [14] used the fluid–structure coupling framework HAWC2CFD to study the inflow and operating conditions of a reference NREL 5 MW wind turbine. In addition, they also conducted a study on aeroelastic instability caused by blade-induced vortex vibration on a reference DTU 10 MW wind turbine [3]. B. Dose [15] and others combined the open-source computational fluid dynamics (CFD) code OpenFOAM in version 4.1.0 and the internal structure solver BeamFOAM to calculate the aeroelastic response of the NREL 5 MW reference wind turbine under various conditions and used the solver framework to study the influence of blade deformation on key aerodynamic parameters such as power, thrust and cross-sectional force. At this stage, as the diameter of the wind turbine impeller increases, the aeroelastic effect becomes more and more obvious, and the limitations of the engineering algorithm become more and more obvious. In order to be able to realize a geometric nonlinear analysis of large blade deformations, improve the reliability of an aeroelastic simulation of blades and meet the calculation accuracy and efficiency requirements, it is necessary to establish a two-way fluid–structure coupling model to meet the above requirements.

Currently, the methods used for structural dynamics analyses of wind turbine blades mainly include modal analyses, the finite element method, and the multi-body dynamics method [16]. The modal analysis method has a high computational efficiency, but the obtained modes are often based on the assumption of a small deformation and a linear model analysis. Therefore, it cannot meet the requirement of a geometric nonlinear analysis for long and flexible wind turbine blades. The multi-body dynamics method [17] can accurately simulate wind turbine rotation conditions, but the constructed dynamic equations are relatively complex, resulting in a lower computational efficiency for the aerodynamic elastic analysis of blades under standstill conditions. Savino A. et al. [18] combine multi-body structural modeling with a mid-fidelity numerical representation of the aerodynamics, which enabled them to accurately capture aerodynamic interaction effects in rotorcrafts. Cocco A. et al. [19] proposed a method for a stability analysis of systems under periodic aerodynamic excitation using a full-featured multibody solver. Leng J. et al. [20] analyze turbine aeroelastic performance and fluid–structure interactions based on large eddy simulations of flexible multibody dynamics and the anisotropic actuator line method. It is shown that the method is effective in predicting wind turbine performance measures, such as deformation and power output.

Research on the aeroelasticity of typical slender flexible structures like wind turbine blades can utilize a geometrically exact beam model within the framework of finite element methods [21,22], which has been widely applied in the field of helicopter rotor blades [23]. In research by Hsu, M. C. et al. [24], the finite element formulation ALE-VMS was used to simulate

a rotor with a full configuration of the wind turbine under a wide range of wind conditions, and the simulation results were in good agreement with the experimental data. Jensen, F. M. et al. [25] conducted large-scale cyclic loading tests on two blade cutouts through tests and found that both blades underwent structural damage Additionally, the effect of torsional loading on the current structural failure modes associated with large wind turbine blades was investigated by performing nonlinear geometric 3D finite element simulations. Geometrically exact beams directly establish the strain displacement relationship under large rotational deformations, addressing finite rotation issues through appropriate the choice and design of interpolation and integration methods. Qian et al. [26] calculated the dynamic response of an IEA 15 MW blade under steady wind and turbulent conditions using a linear geometrically exact beam method. They validated the accuracy of the geometrically exact beam model by employing a cantilever beam case study with pre-bending. Therefore, in this paper, the geometrically exact beam model is employed to solve the structural domain in the coupled model. This paper establishes a coupling method with a high level of precision and at a relatively low cost. Specifically, it solves the nonlinear structural motion equations using the geometrically exact beam method while computing flow field parameters using CFD methods. Meanwhile, interpolation methods and data transfer methods are established between the aerodynamic force and structural beam models, forming a coupled model to calculate and analyze the aeroelastic characteristics of wind turbine blades under standstill conditions.

2. CFD-CSD Coupling Simulation Method

The establishment of a coupled computational framework for aeroelasticity fundamentally relies on the seamless exchange of data between the flow solver and the structural solver, ensuring the alternation between these two processes. The methodology of this paper is based on two-way loosely coupled iterative solving of the flow solver and the structural solver at small time steps. Figure 1 illustrates the coupling principle of the fluid–structure coupling computational procedure in this study. The coupling procedure begins with the operation of the fluid computation module, which calculates the velocity field, pressure field, etc., over the entire computational domain. Based on the computed flow parameters, such as the velocity field, aerodynamic forces are calculated on the grid. These aerodynamic force data are then transferred to the structural computation module, in which the structural solver calculates the structural deformations. The flow solver reads the deformation data transmitted by the structural solver, deforms the grid, and computes parameters such as the velocity field based on the deformed grid. This completes one time step of the coupling process, which iterates until the set total simulation time is reached.

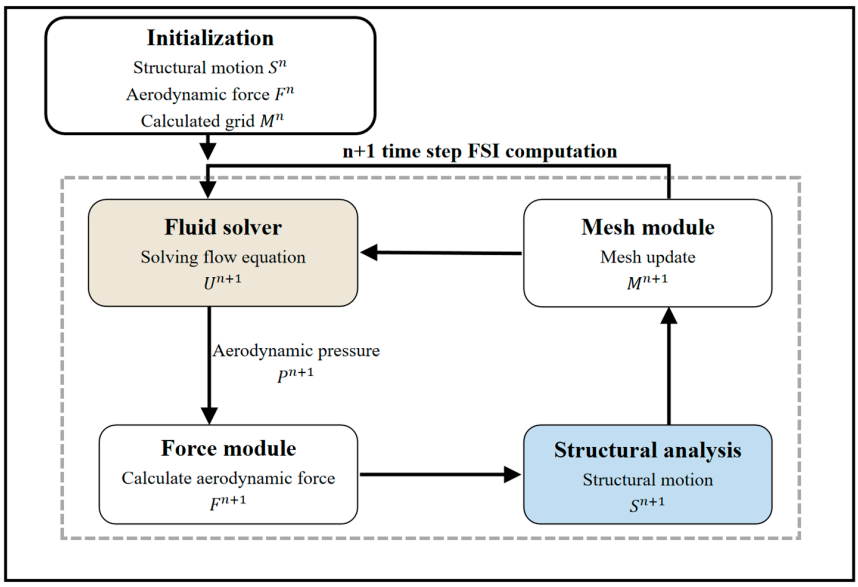

Figure 1. Schematic diagram of the coupling principle of fluid–structure coupling calculation.

2.1. Flow Solver

For the aeroelastic simulation of wind turbine blades under standstill conditions, the calculation in this paper uses a pressure-based solver suitable for solving for low-speed incompressible flow. The standard k-ε model is used as the turbulence model for the calculation. The spatial discretization format adopts the first-order upwind format and the time discretization The format adopts a first-order accuracy time discretization format. The calculated turbulence model, as well as the space and time discretization formats are introduced below.

The standard k-ε model is a classical two-equation turbulence model that describes both length and time scales of turbulence by solving two discrete transport equations. Due to its robustness, computational efficiency and ability to yield a reasonable accuracy across a wide range of turbulent flows, this model is widely employed in engineering practice for solving various flow problems.

2.1.1. Turbulence Model

The standard k-ε model is founded upon the transport equations that govern the turbulent kinetic energy (k) and its dissipation rate (ε). Within this model, the fluid is presumed to be fully turbulent, thereby disregarding the effects of molecular viscosity. The governing equations for the turbulent kinetic energy (k) and its dissipation rate (ε) are enumerated as follows:

$$\frac{\partial}{\partial t}(\rho k) + \frac{\partial}{\partial \chi_i}(\rho k u_i) = \frac{\partial}{\partial \chi_j}\left[\left(\mu + \frac{\mu_t}{\sigma_k}\right)\frac{\partial \varepsilon}{\partial \chi_j}\right] + G_k + G_b - \rho\varepsilon - Y_M + S_k \quad (1)$$

$$\frac{\partial}{\partial \mathrm{t}}(\rho\varepsilon) + \frac{\partial}{\partial \chi_{\mathrm{i}}}(\rho\varepsilon \mathrm{u_i}) = \frac{\partial}{\partial \chi_{\mathrm{j}}}\left[\left(\mu + \frac{\mu_{\mathrm{t}}}{\sigma_{\mathrm{k}}}\right)\frac{\partial \varepsilon}{\partial \chi_{\mathrm{j}}}\right] + \mathrm{C}_{1\varepsilon}\frac{\varepsilon}{\mathrm{K}}(\mathrm{G_k} + \mathrm{G}_{3\varepsilon}\mathrm{G_b}) - \mathrm{C}_{2\varepsilon}\rho\frac{\varepsilon^2}{\mathrm{K}} + \mathrm{S}_\varepsilon \quad (2)$$

In the above two equations, G_k represents the overall turbulent kinetic energy due to mean velocity gradients, G_b represents the turbulent energy induced by buoyancy and Y_M represents the fluctuating expansion's contribution to the total dissipation rate of the compressible turbulence. The expressions for these three terms are as follows: $C_{1\varepsilon}$, $C_{2\varepsilon}$ and $C_{3\varepsilon}$ are constants, σ_k and σ_ε are the turbulence Prandtl numbers for k and ε, respectively, and S_k and S_ε are custom-defined source terms.

2.1.2. Spatial Discretization Scheme

In the course of the solution process, the variables obtained are conventionally stored at the centers of the control volumes. Nevertheless, acquiring the variable values on the faces of these control volumes is equally imperative. Spatial discretization is accomplished with a first-order upwind scheme, which exhibits first-order accuracy. This scheme rests on the premise that the values at the center of the control volume represent the average value within the entire volume, and that the variable values across the entire control volume are equivalent to these central values. Consequently, within the first-order upwind scheme, the variable value on the boundary face of a control volume is approximated by the center value of the upstream control volume.

2.1.3. Temporal Discretization Scheme

For unsteady computations, discretization is required not only in space but also in time. The general expression for the temporal evolution of a variable is as shown in Equation (3):

$$\frac{\partial \varphi}{\partial \mathrm{t}} = \mathrm{F}(\varphi) \quad (3)$$

where F represents any spatial discretization term. Assuming the time derivative is approximated using a backward differencing method, the first-order accurate temporal discretization format is as follows:

$$\frac{\varphi^{n+1} - \varphi^n}{\Delta t} = F\left(\varphi^{n+1}\right) \quad (4)$$

In Equation (4), the time derivative has been discretized, where $F(\varphi^{n+1})$ represents the value at the next time step, i.e., the $(n + 1)$th time step. This method is an implicit time iteration method.

2.1.4. Verification of CFD Method

To validate the efficacy of the CFD method proposed in this paper, we computed the dynamic stall aerodynamic forces of the widely used S809 airfoil in wind turbine applications. According to experiments conducted in references [27,28], the S809 airfoil was subjected to pitching motion with an average angle of attack of 8.25°, amplitude of 10.15° and reduced frequency of ks = 0.02. The Reynolds number was set to Re = 1,000,000. We compared the computed dynamic aerodynamic force response under this pitching motion with experimental results. Since the experimental measurement of aerodynamic forces employed surface pressure distribution measurements, the measured drag only includes the pressure drag and cannot accurately measure the viscous drag. In contrast, the computed drag includes the viscous drag. Therefore, the experimental and computed drag data are not directly comparable. Hence, only the lift coefficient is compared here. The analysis results are shown in the figure below.

Figure 2 illustrates the variation in the lift coefficient of the airfoil over time and with the oscillation angle, obtained using the CFD method under the prescribed pitching harmonic motion, along with its comparison with experimental data. From Figure 2, it can be observed that the computed dynamic stall aerodynamic response of the S809 airfoil in this paper closely matches the experimental results in the linear region. However, in the stall region, the computed results are slightly higher than the experimental results. Several factors may contribute to this discrepancy, including the limited capability of the turbulence model used in the CFD method to accurately simulate actual turbulence and the experimental model being a two-dimensional airfoil section, which differs somewhat from the computed two-dimensional airfoil. Nonetheless, the computed results in this work fit well with the experimental results in terms of the intersection points of the two curves and the overall trend of aerodynamic force variation. Therefore, the method employed in this paper meets the requirements of the research.

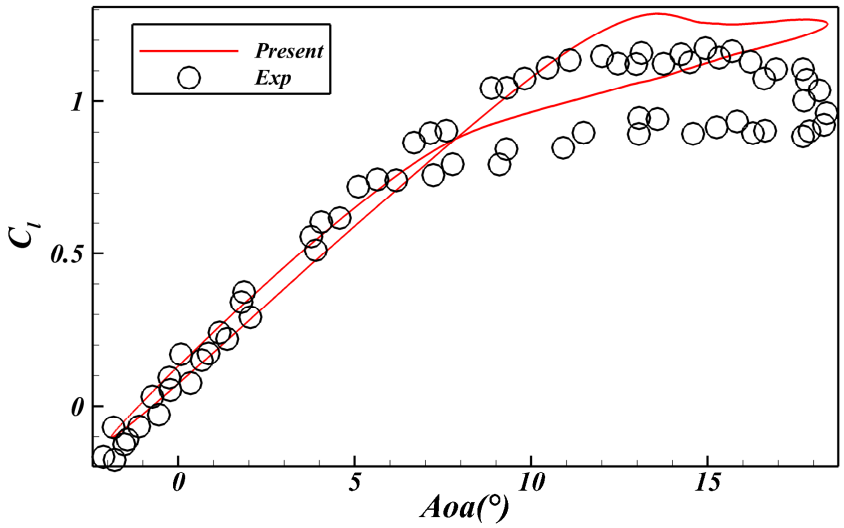

Figure 2. Comparison of dynamic stall aerodynamic response.

2.2. Structural Analysis

The structural solver adopts GTsim (version 1.1.10.3), a whole-turbine dynamic simulation software independently developed by Beijing Goldwind Science & Creation Windpower Equipment Co., Ltd., Beijing , China. GTsim evaluates damping using modal identification methods [29,30], establishes nonlinear differential-algebraic equations based on

the Timoshenko beam theory [31], the co-rotational formula [32,33], and the Newton–Euler motion equation, and employs floating co-rotational transformations to make the rotor isotropic with respect to the rotation center. Furthermore, it utilizes the MBC transformation [34] to obtain time-invariant systems and solves generalized eigenvalue problems using the Krivlov–Schur eigenvalue method [35].

2.2.1. Geometrically Exact Beam Theory

The geometrically exact beam theory is derived from the Timoshenko beam theory based on the assumption of a flat cross-section; the quaternion method is employed to characterize the movement and rotation of the flat cross-section [36] using Equation (5) as follows:

$$\hat{q} = (q_0, q) = (q_0, q_1, q_2, q_3) \tag{5}$$

where q_0 is the scalar part of the quaternion $\hat{q}$, and $[q_1, q_2, q_3]$ is the vector part of $\hat{q}$.

The equations of motion, derived from the virtual work principle [37], and the virtual work of the internal forces can be integrated into Equation (6) as follows:

$$\delta W \int \left(\delta u'^T \Lambda N + \delta \theta^T \widetilde{u}'^T \Lambda N + \delta \theta'^T \Lambda M \right) dZ_{int} \tag{6}$$

where $\wedge$ is the rotation tensor along the reference line of the beam element.

$$\Lambda = \begin{bmatrix} q_0^2 + q_1^2 + q_2^2 + q_3^2 & 2(q_1 q_2 - q_3 q_0) & 2(q_1 q_3 + q_2 q_0) \\ 2(q_1 q_2 + q_3 q_0) & q_0^2 - q_1^2 + q_2^2 - q_3^2 & 2(-q_1 q_0 + q_2 q_3) \\ 2(q_1 q_3 - q_2 q_0) & 2(q_1 q_0 + q_2 q_3) & q_0^2 - q_1^2 - q_2^2 + q_3^2 \end{bmatrix} \tag{7}$$

The virtual work performed by the external aerodynamic forces and gravitational forces can be evaluated using Equation (8) as follows:

$$\delta W_{ext} = \int \left(\delta u^T f_a + + \delta \theta^T \Lambda \widetilde{\overline{R}}_a f_a + \delta \theta'^T m_a \right) dZ + \int \left(\delta u^T A_\rho + + \delta \theta^T A_\rho \Lambda \widetilde{\overline{R}}_g g \right) dZ \tag{8}$$

The virtual work performed by the external aerodynamic forces and gravitational forces can be evaluated using Equation (9) as follows:

$$\delta W_{ext} = \int \delta u^T A_\rho \ddot{u}_g dZ + \int \delta \theta^T \left(A_\rho \Lambda \widetilde{\overline{R}}_g \ddot{u}_g + I_\rho \ddot{\theta} + \widetilde{\dot{\theta}} I_\rho \dot{\theta} \right) dZ \tag{9}$$

The summation of the virtual work of internal forces, external forces and inertial forces is zero, leading to the balance equation of motion using Equation (10) as follows:

$$\delta W_{int} - \delta W_{ext} + \delta W_{inert} = 0 \tag{10}$$

The detailed process to substitute Equations (6) to (10) into the element-discretized balance equations is outlined in the literature [38].

2.2.2. Verification and Validation of the Structural Model

The simulation design capability of GTsim has been extensively verified through comparisons with Bladed, and it has undergone comprehensive simulation tests and targeted optimizations for blade models, drivetrain models and overall system stability models. Figures 3 and 4 present comparisons of root load between GTsim, Bladed and test data on a megawatt commercial turbine, demonstrating that the root edgewise and flapwise moments computed by GTsim align well with field measurements.

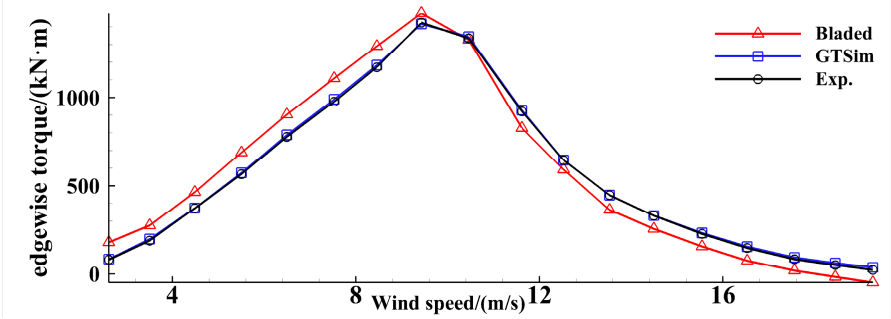

Figure 3. Comparison of blade root torque in the edgewise direction.

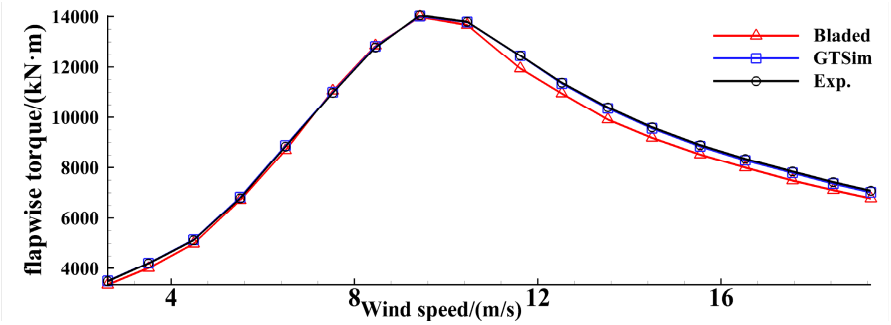

Figure 4. Comparison of blade root torque in the flapwise direction.

The measurement campaign is carried out on turbine with a 160 m rotor diameter. Figure 5 shows the target turbine and its surrounding environment. The test site is located in the southeast of Hami (city), Xinjiang (province). The average altitude is about 950 m above sea level. The site has a flat terrain and is characterized as arid with poor vegetation.

Figure 5. Photo of measurement turbine.

2.3. Grid Interpolation and Deformation Techniques

The implementation process of grid interpolation and deformation techniques is illustrated in Figure 6. The realization of grid mapping and deformation techniques requires establishing the correspondence between beam nodes and three-dimensional surface grids, i.e., identifying the control beam nodes (i.e., blade element centers) of a certain aerodynamic grid. Based on this correspondence, the deformation quantities on the structure are interpolated to these control points, obtaining the deformation quantities controlling a certain aerodynamic grid element. Subsequently, these deformation quantities are applied to the aerodynamic grid, facilitating both three-degrees-of-freedom rotational and three-degrees-of-freedom translational motions, thereby achieving the overall deformation of the surface grid. By employing dynamic grid techniques, the surface grid is associated with the volume grid, enabling the deformation of the fluid solution domain. This section primarily focuses on beam node aerodynamic force interpolation, mapping and deformation interpolation between blade element centers and beam nodes, and aerodynamic surface grid deformation methods.

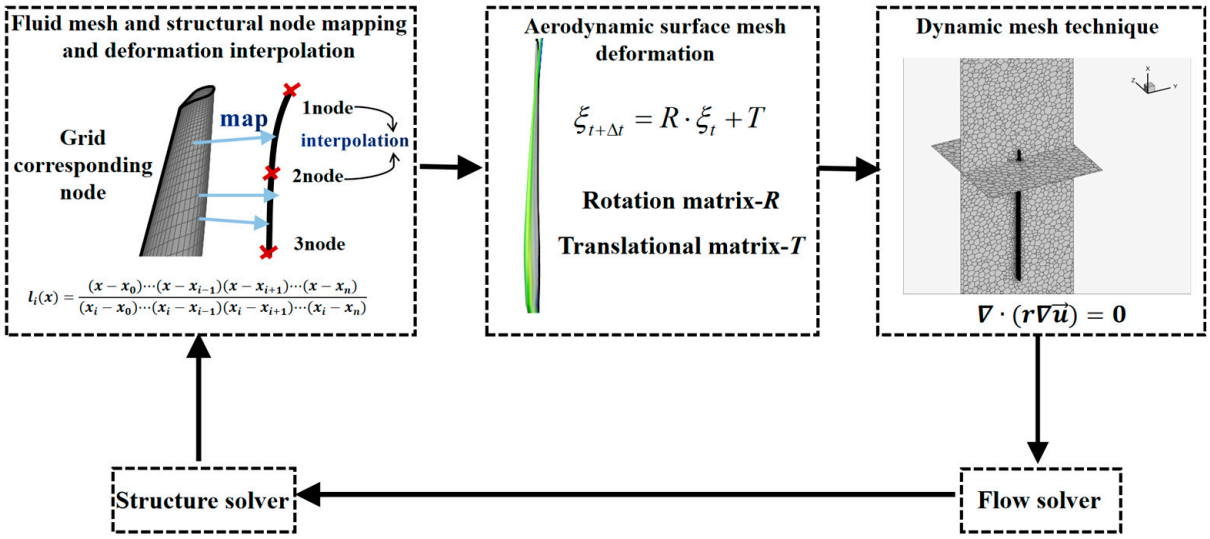

Figure 6. Implementation flow of mesh interpolation and deformation technology.

2.3.1. Beam Node Aerodynamic Force Integration

In the proposed methodology of this paper for fluid–structure coupling computations, it is essential to interpolate the aerodynamic force results obtained from the fluid solver onto the beam nodes. Interpolating the beam node displacements onto the fluid grid involves mapping a large number of nodes with a small amount of data points. Conversely, mapping the aerodynamic force results from the aerodynamic grid onto a small number of beam nodes constitutes an integration process. In fact, all aerodynamic force results obtained in the CFD method of this study are stored at the grid centers; thus, the aerodynamic force mapping relations are based on the grid cell centers. Figure 7 illustrates the correspondence between the integration grid and beam nodes, where O_{n-1}, O_n and O_{n+1} represent the beam nodes, and the shaded area on the left side of the blade corresponds to the integration region of the aerodynamic grid associated with O_n. The criterion for determining whether a grid contributes aerodynamic forces to a beam node based on the x-coordinate of the grid center is shown in Equation (11) as follows:

$$(X_f - X_n) \cdot (X_f - X_{n+1}) \leq 0 \tag{11}$$

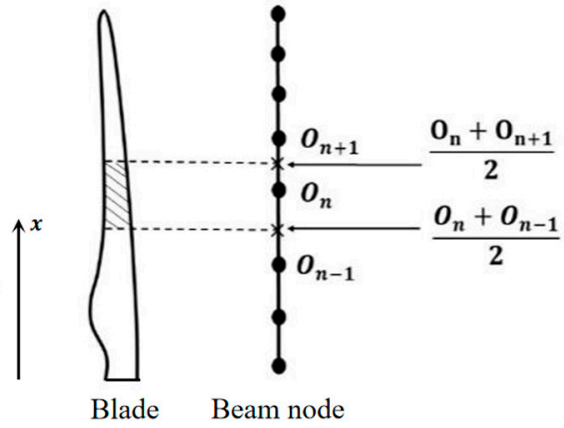

Figure 7. Integral mapping of aerodynamic force from grid to beam node.

In the equation, X_f represents the x-coordinate of the center of grid f, X_n represents the x-coordinate between O_n and O_{n-1}, and X_{n+1} represents the x-coordinate between O_n and O_{n+1}. If the criterion is satisfied, grid f contributes to the aerodynamic force of beam node O_n. Finally, summing up the aerodynamic forces from all grid cells contributing to O_n yields the aerodynamic force at beam node O_n.

2.3.2. Mapping and Displacement Interpolation between Blade Element Centers and Beam Nodes

Due to the large slenderness ratio of wind turbine blades, the first-order beam model can be employed as the theoretical model for computing structural displacements, as illustrated in Figure 8a. The left side depicts the actual blade, while the right side depicts the simplified beam nodes. Assuming the beam nodes are located at the blade element centers, the curve formed by connecting all beam nodes is defined as the blade element center curve. Furthermore, assuming the blade is parallel to a certain coordinate system, designated as the *x*-axis, a perpendicular line drawn from a point P on the blade to the blade element center curve intersects at point O. Point O, the intersection point of the perpendicular line and the blade element center curve, represents the blade element center for point P, with the x-coordinate of point P being equal to that of structural point O.

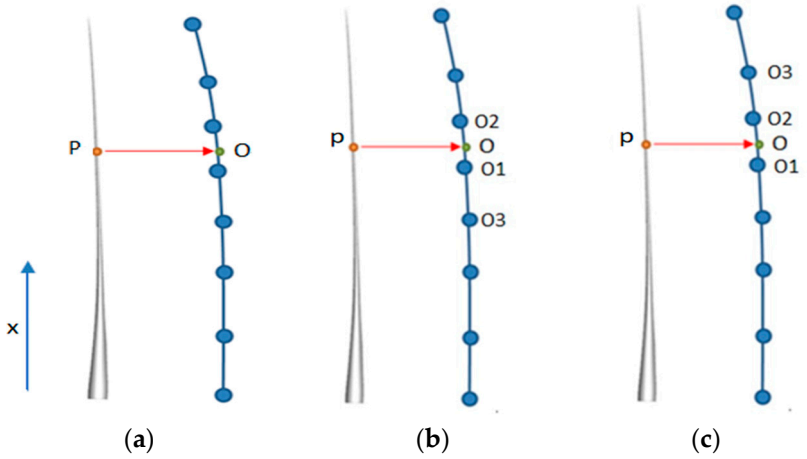

Figure 8. (**a**) The selection method of the corresponding points of blade elements on the beam nodes of the surface grid. (**b**,**c**) Different selection policies for O3.

Since the number of beam nodes transmitted from the solver is only a few dozen, the blade element centers corresponding to each blade grid need to be obtained through interpolation using existing beam nodes. This paper adopts the three-point Lagrange interpolation method, which requires using three known points to interpolate the information

of the unknown point O. Assuming point O lies between O1 and O2, there are two methods for selecting O3, as illustrated in Figure 8b,c. The selection principle for O3 can be based on the difference in x-axis coordinates with point P, in which O3 is chosen as the point with the smallest difference in x-coordinates with point P among the two cases. Specifically, for positions near the blade root and tip, three adjacent beam nodes can be selected. Once O1, O2 and O3 are determined, their x-coordinates are set as independent variables, and based on the three-point Lagrange interpolation basis functions, the interpolation basis function for point O can be derived as shown in Equation (12) as follows:

$$l_j(x) = \prod_{i=0, i\neq j}^{3} \left(\frac{x - x_i}{x_j - x_i} \right) = \left(\frac{x - x_0}{x_j - x_0} \right) \left(\frac{x - x_1}{x_j - x_1} \right) \left(\frac{x - x_2}{x_j - x_2} \right) \tag{12}$$

2.3.3. Aerodynamic Surface Mesh Deformation

The key to realizing fluid–structure coupling lies in the data exchange between the fluid solver process and the structural solver process. On the fluid solver side, the node displacements transmitted from the structural solver are used to deform the grid based on the mapping relationship between the beam nodes and the blade grid, as described earlier. Subsequently, new aerodynamic forces on the deformed grid are computed under the transformed grid and then transmitted back to the structural solver. To update the computational grid, it is necessary to map the information of the blade element centers described in Section 2.3.2 to the blade surface.

The blade can be regarded as a solid composed of numerous airfoil cross-sections (blade elements). Each point on the blade surface corresponds to a specific cross-section. The motion of any point on the blade surface can be described by the combination of rotation and translation around the blade element center. Therefore, for any point on the blade surface, it is only necessary to know its corresponding blade element center, along with the rotation angle and translation displacement of the blade element center. By using quaternions to construct rotation matrices and translation matrices, the coordinates of all aerodynamic grid points after deformation can be computed.

For instance, consider a point P on the blade surface, whose motion process is illustrated in Figure 9. The expression for the displacement vector of its motion is given by Equations (13) and (14) as follows:

$$P''O' = P'O + \vec{T} \tag{13}$$

$$P'O = R * PO \tag{14}$$

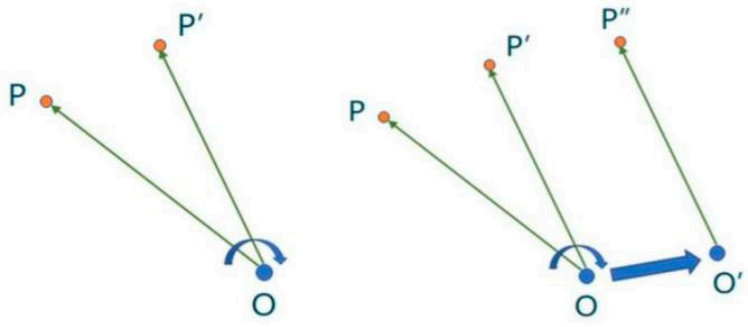

Figure 9. Trajectory of a certain point on the blade.

Suppose the blade element is rotated by angle a and translated by distance l. Here, R represents the rotation matrix. PO denotes the original vector; P′O represents the displacement vector of point P after rotating around point O by angle a, mathematically expressed as the vector PO multiplied by the rotation matrix R; and $\vec{T}$ denotes the translation vector. P″O represents the final displacement vector of point P′ after being translated by distance l,

mathematically expressed as the vector P′O added to the translation vector $\vec{T}$, resulting in the final displacement vector P″O′.

3. Simulation Setup

3.1. Introduction of Single-Blade Parameters and Calculation Conditions

The model of this paper is a single wind turbine blade with a length of 124 m. The first four modal frequencies of this blade are calculated and compared with the results of the wind turbine simulation software, Bladed (version 4.11), as shown in Table 1. The maximum deviation occurs in the calculation results of the second-order flapwise frequency, with a deviation of 1.03%. The aeroelastic instability vibration of the wind turbine blade under standstill conditions tends to be dominated by the first-order edgewise mode frequency. The deviation of the first-order edgewise frequency is 0.21%, and the error of the first-order edgewise frequency is 0.51%, which shows that the calculation results have a high level of credibility.

Table 1. First four orders of structural frequency.

Modal Frequency	Bladed Hz	GTsim Hz	Deviation %
First flapwise mode	0.2969	0.2984	0.51
First edgewise mode	0.4157	0.4165	0.21
Second flapwise mode	0.8779	0.8869	1.03
Second edgewise mode	1.2577	1.2629	0.42

Figure 10 shows the model diagram of the blade. Figures 11 and 12 show the mesh of the blade at the root and the tip, respectively. The computational domain mesh is divided by tetrahedral unstructured meshes, the total number of which is 10,256,340. The schematic diagram of the incoming flow condition is shown in Figure 13, and the size of the actual computational domain is 1680 × 240 × 240 m. The computational model is a single wind turbine blade, in which the root of the blade is fixed, the tip of the blade is free and the blade is placed horizontally. The aeroelastic analysis is carried out when the incoming wind blows from the tip of the blade to the root of the blade. The angle of the incoming flow wind is 90°, and the azimuthal angle is 270°.

Figure 10. Blade model.

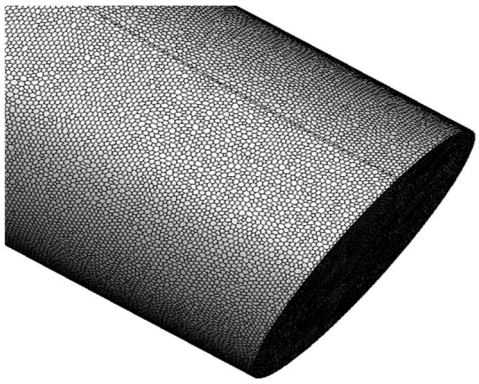

Figure 11. Surface grid at blade root.

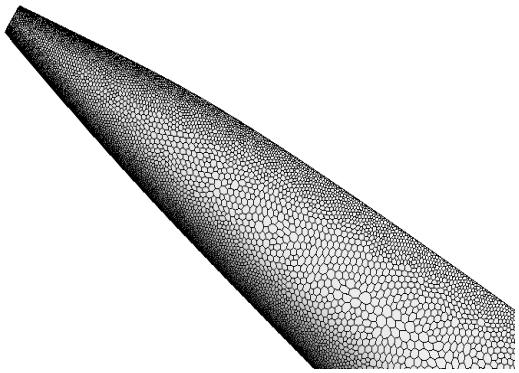

Figure 12. Surface grid at blade tip.

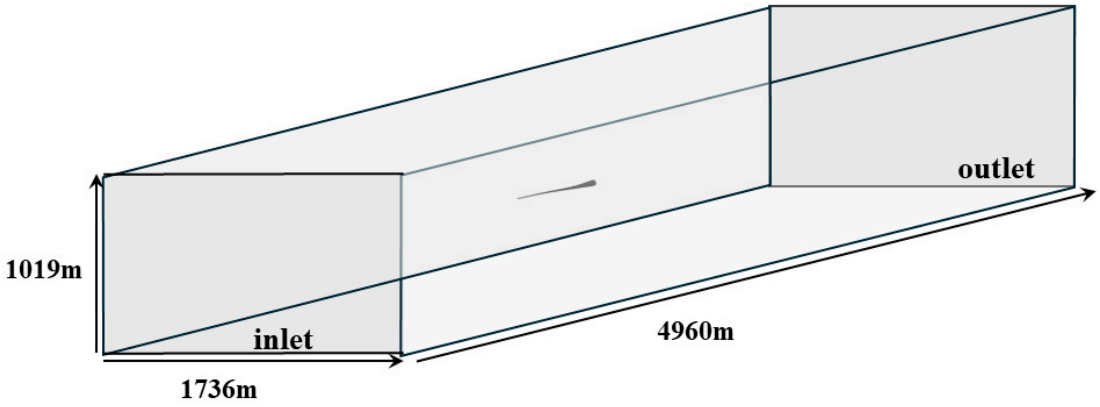

Figure 13. Schematic diagram of simulation case conditions.

Table 2 shows the three different operating conditions under which the aeroelasticity calculations are carried out and the setting of the two parameters (turbulence intensity and gravity) this study mainly focuses on.

Table 2. Simulation case conditions.

Calculate Working Conditions	Wind Speed $m \cdot s^{-1}$	Turbulence %	Gravity
A	35	0.01	disregard
B	35	0.01	regard
C	35	10	regard

3.2. Method Verification

Figures 14 and 15 compare the simulation results of the flapwise moments at the blade root calculated by the CFD-CSD coupling method in this paper and the engineering simulation software Bladed based on the BEM/modal superposition method under low-turbulence condition B and high-turbulence condition C, respectively. It can be seen that there are differences between the two methods in the calculation of the amplitude of the flapwise moment. But in the frequency domain analysis, the dominant frequencies of the flapwise moment obtained by the two methods are consistent with the first-order flapwise frequency of the blade, which illustrates the consistent accuracy of the two methods for the simulation of the blade's aeroelastic vibration frequency. Therefore, it can be considered that the CFD-CSD coupling method in this paper has a high level of confidence in the aeroelastic simulation of the blade.

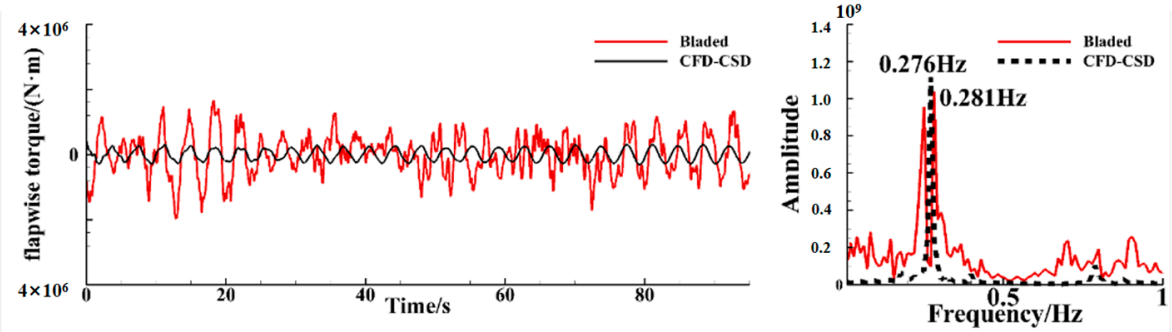

Figure 14. Comparison between Bladed and the CFD-CSD method of this paper for the calculation of blade root flapwise moment for B operating condition.

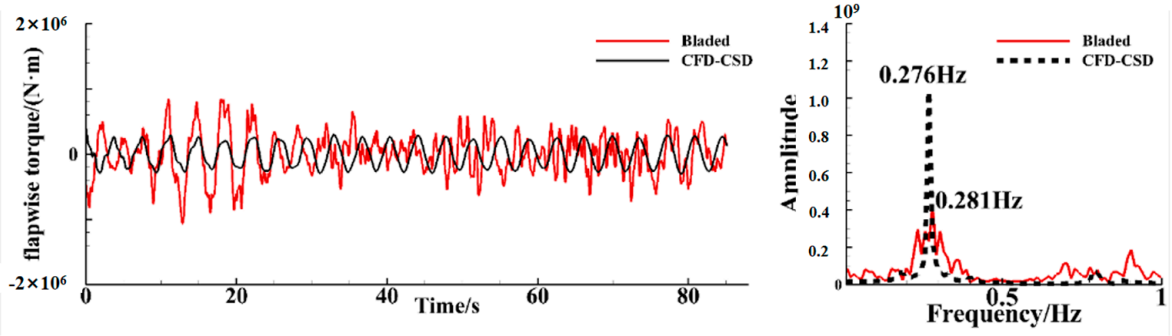

Figure 15. Comparison between Bladed and the CFD-CSD method of this paper for the calculation of blade root flapwise moment for C condition.

4. Results and Discussion

4.1. Analysis of Single-Blade Simulation Results

The following figures show the time-domain responses of the edgewise vibration and flapwise vibration deformation at the blade tip and the corresponding spectral analyses under different conditions. In Figure 16, under condition A, there are two peak frequencies of 0.267 Hz and 0.400 Hz in the edgewise vibration frequency domain plot. The latter one, which is close to the blades's first-order edgewise modal frequency, shows a larger contribution. So the blade vibration response frequency corresponds to the structural mode frequency. For case B in Figure 17, when only taking the influence of gravity into consideration, the response in the direction of the edgewise vibration is divergent, with an amplitude of about 4.5 m, and the main frequency of vibration is 0.419 Hz, which is in line with the first-order edgewise mode frequency of the blade. For Case C in Figure 18, which considers both the effects of gravity and turbulence intensity, the results are similar to those of Case B. The response diverges, and the dominant frequency is 0.417 Hz, which is consistent with the first-order edgewise mode frequency of the blade. Comparing Figures 16 and 17, it can be seen that the amplitude of the vibration response in the direction of the edgewise vibration increases significantly after considering the effect of gravity. As shown in Figure 19, when keeping other incoming flow parameters unchanged, the increase in the turbulence intensity does not cause a huge change in the edgewise deformation of the blade tip. In the two different working conditions, the frequencies of vibration are observed to be 0.420 Hz and 0.417 Hz, respectively. It can be inferred that the vibration frequency consistently aligns with the first-order edgewise vibration frequency.

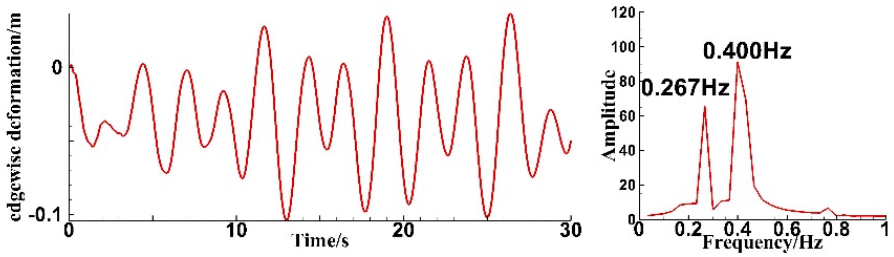

Figure 16. Time–frequency diagram of blade tip edgewise deformation under condition A.

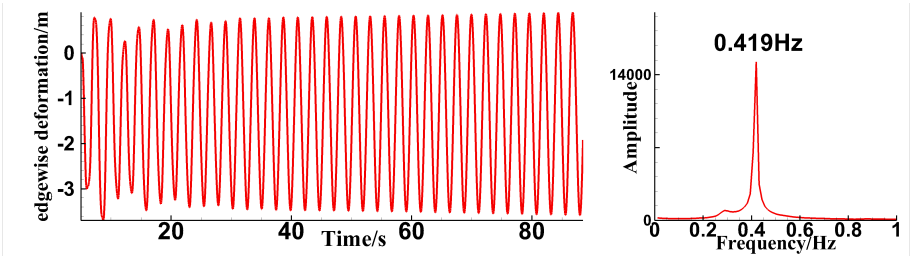

Figure 17. Time–frequency diagram of tip edgewise deformation under condition B.

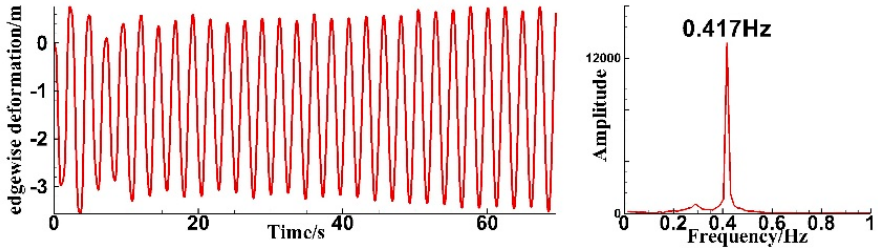

Figure 18. Time–frequency diagram of tip edgewise deformation under condition C.

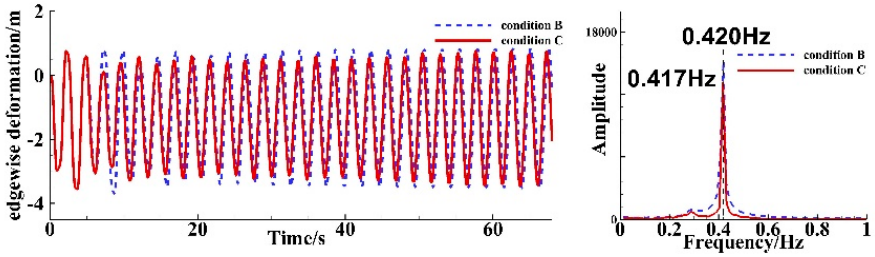

Figure 19. Comparison of tip edgewise deformation under conditions B and C.

Figure 20 shows the time–frequency diagram of the blade tip flapwise deformation under condition A. An obvious vibration divergence phenomenon occurs, with a relatively small amplitude. And the main frequency of vibration is 0.267 Hz, which is similar to the first-order flapwise frequency. Figure 21 shows the time–frequency diagram of the tip flapwise deformation under working condition B. It can be clearly seen that the vibration amplitude in the flapwise direction converges from the initial large amplitude and then maintains a small amplitude vibration. And at the same time, the frequencies of the initial large amplitude section and the vibration convergence section are obviously different, and there are three peak frequencies of 0.287 Hz, 0.419 Hz, and 0.861 Hz in the frequency domain diagram, corresponding to the first-order flapwise mode frequency, the first-order edgewise mode frequency and the second-order flapwise mode frequency, respectively. Figure 22 shows the time–frequency diagram of the blade tip flapwise deformation for Case C. The results are similar to those of Case B, with the existence of three peak frequencies of 0.288 Hz, 0.418 Hz and 0.864 Hz, and the contribution value of 0.288 Hz is the largest. As shown in

Figure 23, the main frequencies under the two conditions are different during the vibration convergence section, as the one for Case B is 0.423 Hz, which is consistent with the first-order edgewise mode frequency, while the other one for Case C is 0.270 Hz, corresponding to the first-order flapwise mode frequency. This indicates that an increasing turbulence intensity will change the dominant mode in the blade flapwise-direction vibration.

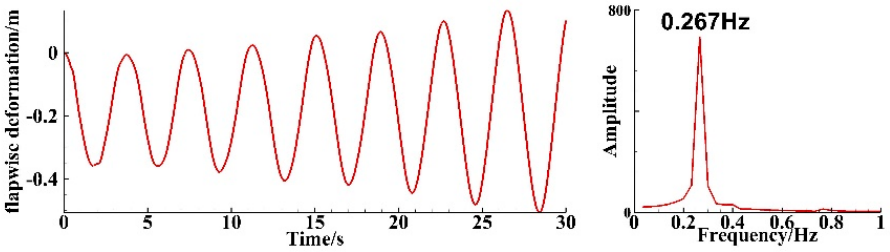

Figure 20. Time–frequency diagram of blade tip flapwise deformation under condition A.

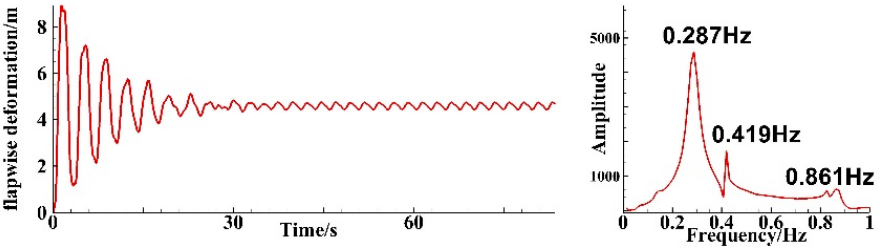

Figure 21. Time–frequency diagram of blade tip flapwise deformation under condition B.

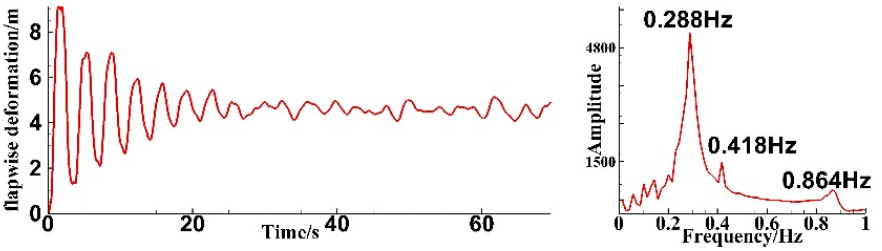

Figure 22. Time–frequency diagram of blade tip flapwise deformation under condition C.

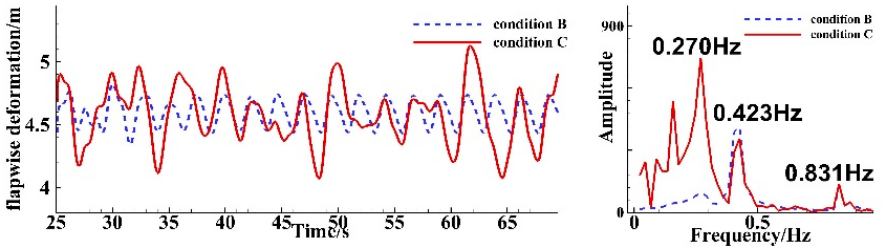

Figure 23. Comparison of tip flapwise deformation under conditions B and C.

In this paper, the forces and moments in the direction of edgewise vibration are also calculated for each working condition based on this CFD-CSD coupling method, as shown in Figures 24–27. It can be clearly seen that the main frequencies of the forces and moments in the direction of edgewise vibration are consistent with the first-order edgewise mode frequency. Comparing the force and moment in the edgewise direction of the blade root in Case B and Case C, the amplitudes and main frequencies of the force and moment in the edgewise direction decrease when the turbulence intensity increases, indicating that increasing the turbulence intensity is beneficial to the stabilization of the aeroelastic response.

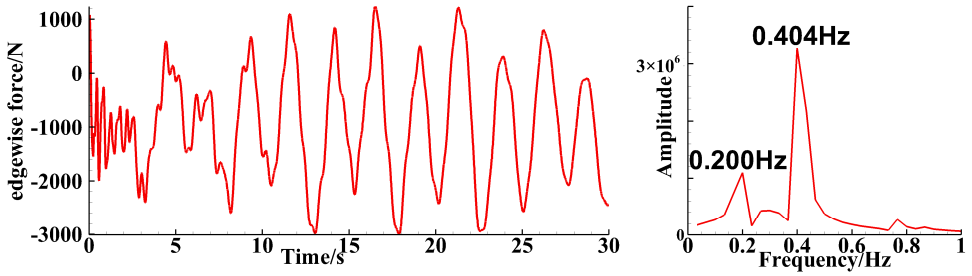

Figure 24. Time–frequency diagram of edgewise-direction force of blade root under condition A.

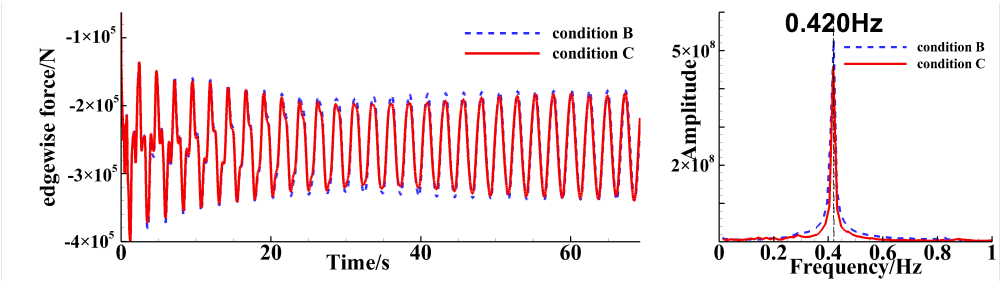

Figure 25. Comparison of edgewise-direction force of blade root under conditions B and C.

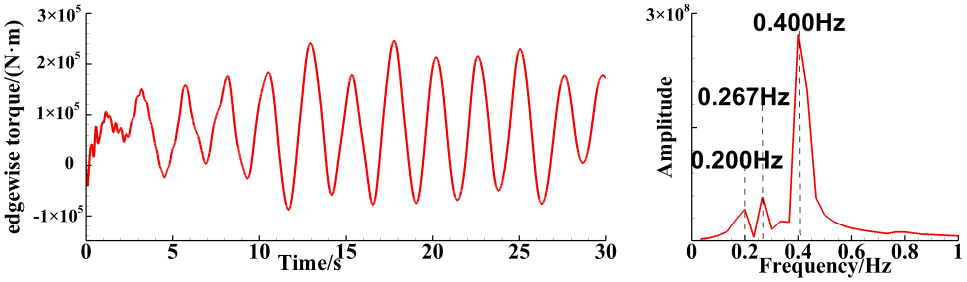

Figure 26. Time–frequency diagram of edgewise-direction moment of blade root under condition A.

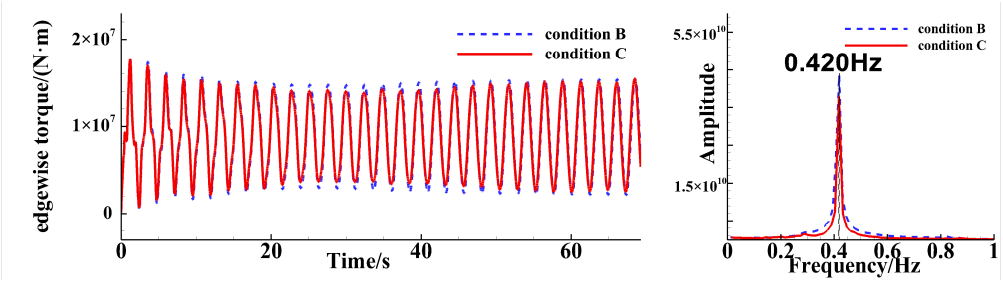

Figure 27. Comparison of edgewise-direction moment of blade root under conditions B and C.

4.2. Analysis of Three-Blade Simulation Results

In this section, the computational model is a three-blade wind turbine rotor model. In the model setup, the structural response of the blades is computed separately without exchanging information through the rotor shaft. The interactions between the three blades, such as the influence of votex shedding induced by the upstream blade on the downstream blade, are only considered during the fluid simulation.

Wherein, blade 1 is vertically upward, with an azimuth angle of 0° and a pitch angle of −50°. The azimuth angles of blade 2 and blade 3 are 240° and 120°, respectively, and the pitch angles are both −90°. The incoming wind angle is 90° and the speed of the uniform incoming flow is 35 m/s. The calculation working condition diagram is shown in Figure 28,

which mainly realizes the simulation and analysis of the blade root bending moment and blade tip deformation of the three blades at different positions.

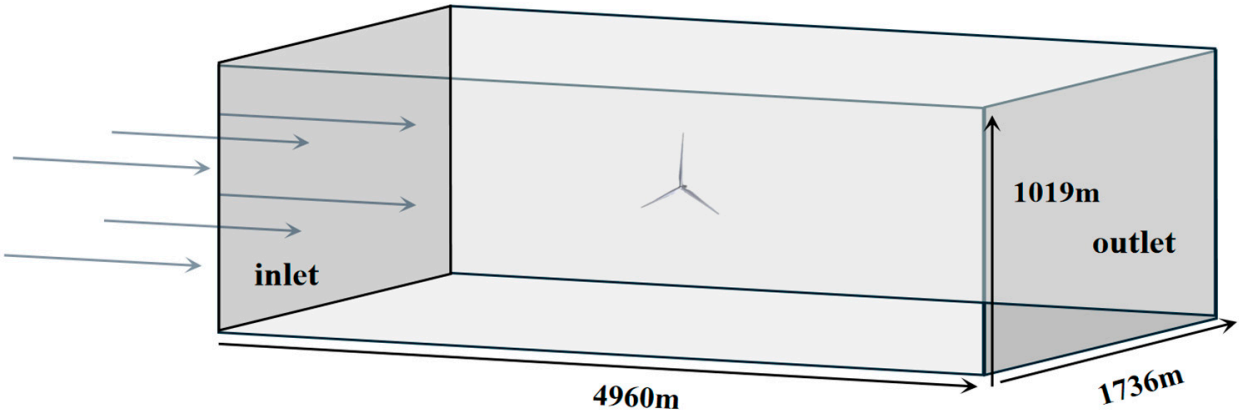

Figure 28. Calculated working conditions of a three-bladed rotor.

4.2.1. Blade Tip Deformation

The following figures show the time-domain response of the edgewise vibration deformation at the tip position of the three blades and the corresponding frequency analysis results. Figure 29 illustrates the time-domain plot of the edgewise vibration deformation of the three blades. Figure 30a shows the time-domain diagram of blade 1's edgewise deformation, indicating significant aeroelastic instability in the edgewise direction. The vibration amplitude eventually reaches approximately 4 m during the simulation time period, and the dominant vibration frequency is 0.414 Hz, consistent with the first-order edgewise frequency of the blade. Figure 30b illustrates the time-domain diagram of blade 2's edgewise deformation. It can be observed that the vibration amplitude of blade 2 increases from 5 s to 15 s during the simulation period, remains stable from 15 s to 35 s and ultimately stabilizes at around 4.85 m. The dominant vibration frequency is 0.419 Hz, consistent with the first-order edgewise mode frequency of the blade. Figure 30c depicts a time-domain diagram illustrating the edgewise deformation of blade 3. It is evident that the edgewise motion of blade 3 exhibits a progressively increasing vibration amplitude over time. The deformation range in the edgewise direction spans from 1.0 to 1.3 m, with a dominant frequency of 0.419 Hz, consistent with the first-order edgewise frequency of the blade. Consequently, this observation suggests that under steady-state inflow conditions, the first-order edgewise frequency of the blade governs the predominant frequency of edgewise motion in the direction of all three blades.

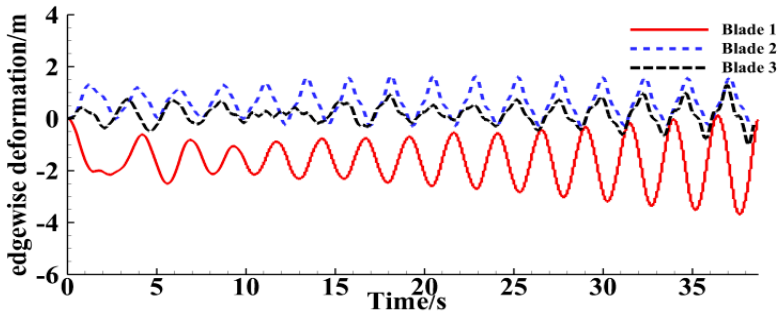

Figure 29. Time-domain plot of the edgewise deformation of the three-blade tip.

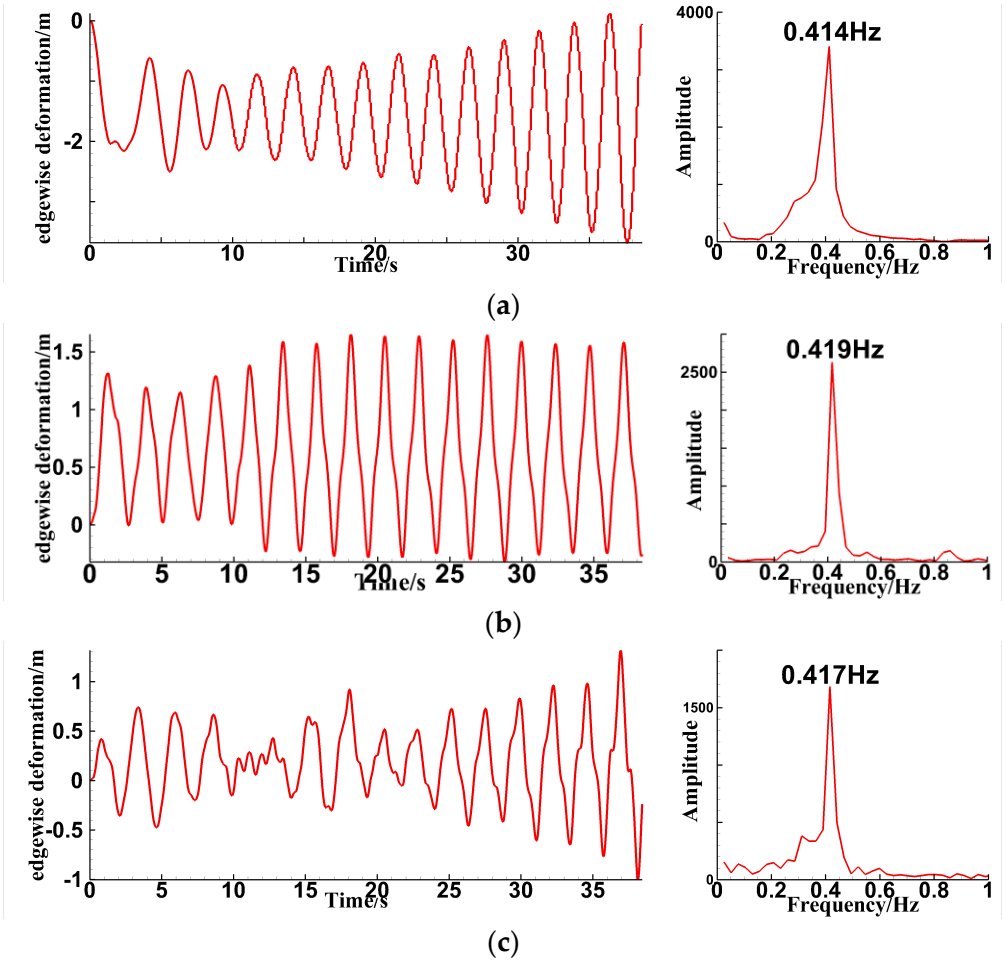

Figure 30. Time–frequency plot of blade tip edgewise deformation. (**a**) blade 1; (**b**) blade 2; (**c**) blade 3.

The accompanying figures illustrate the time-domain response and frequency spectrum analysis of the flapwise vibration deformation at the tip of each blade. Specifically, Figure 31 presents the time-domain plot of the flapwise deformation of the three blades. Figure 32a depicts the time-domain plot of the blade 1 flapwise deformation. It is evident that following a significant initial disturbance, the flapwise direction of blade 1 exhibits coupling between the first-order edgewise mode and the first-order flapping mode from 5 s to 15 s. Consequently, a component of 0.286 Hz emerges in the frequency domain analysis, aligning with the first-order flapwise frequency. Subsequent to the 15-s mark, the first-order flapping mode is subdued, with the predominant vibration frequency registering at 0.413 Hz, signifying the ascendancy of the first-order edgewise mode in the vibration dynamics. Figure 32b displays the time-domain plot of the flapwise deformation of blade 2. It can be observed that following a significant disturbance during the initial phase of vibration, the vibration gradually attenuates to an average deflection of around 9 m. The frequency spectrum analysis of the entire vibration process indicates that during the stabilization phase, there are contributions from both the first and second flapwise modes of vibration. Figure 32c depicts the time-domain plot of blade 1's flapwise deformation. The frequency domain analysis reveals that the dominant frequency of the flapwise vibration in the direction of blade 3 is 0.315 Hz, which matches the frequency of the first-order flapwise mode. This suggests that the vibration is primarily influenced by the first flapwise mode. However, due to the limited simulation time, predictions regarding the subsequent vibration behavior cannot be made.

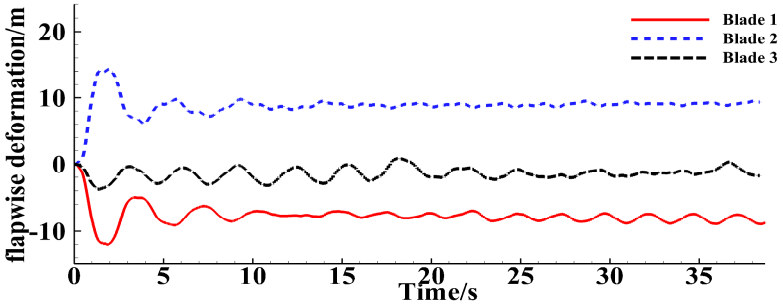

Figure 31. Time-domain plot of the flapwise deformation of the three-blade tip.

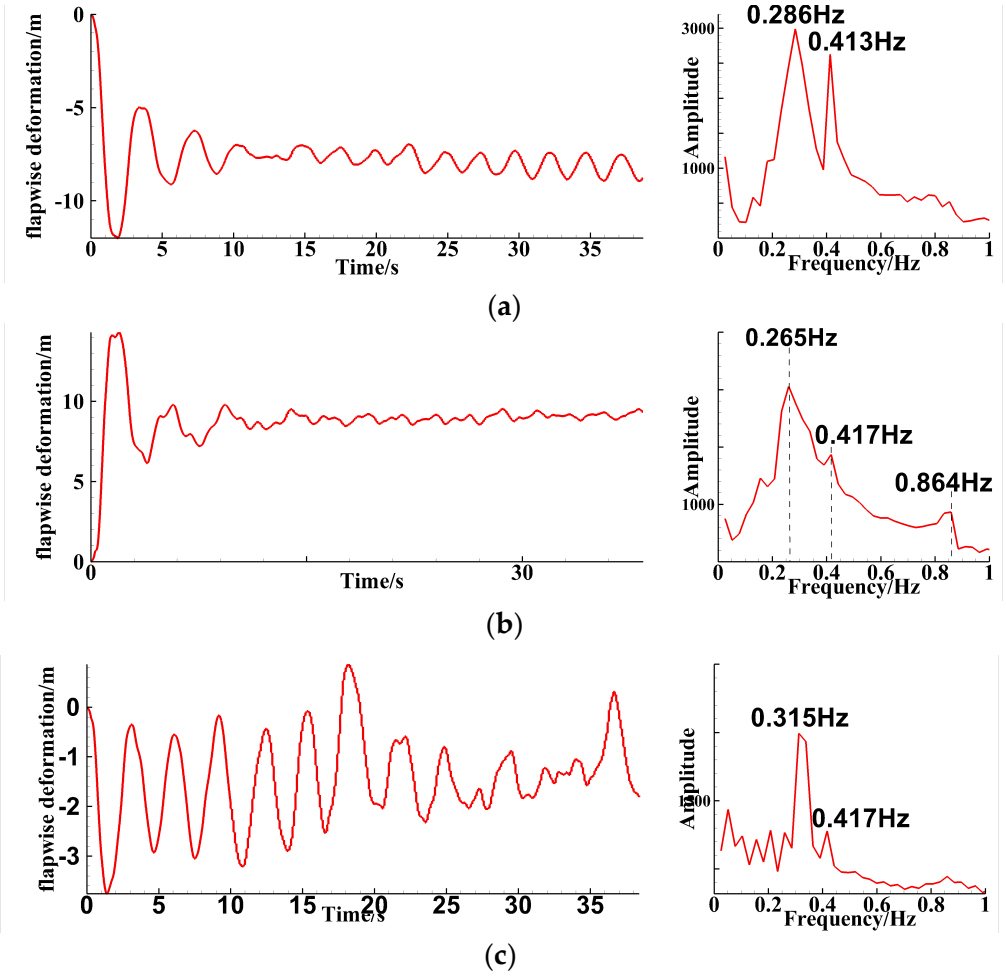

Figure 32. Time–frequency plot of blade tip flapwise deformation. (**a**) blade 1; (**b**) blade 2; (**c**) blade 3.

4.2.2. Root Bending Moment

Figure 33 delineates the bending moments at the root of the three blades in their respective edgewise directions. Due to the distinct positions of the blades within the domain, the behavior of bending moments at the root exhibits variability. Figure 33 illustrates an increasing trend in the edgewise moments of both blade 1 and blade 3 during the simulation process. Figure 34a exhibits the average edgewise-direction moment of blade 1 at 4000 kNm and an approximate magnitude of 3000 kNm at the end of the simulation. Figure 34b,c present the frequency-domain plots of the edgewise-direction moments for blade 2 and blade 3, respectively, indicating the concurrent influence of the first-order and second-order edgewise modes on both blade 2 and blade 3.

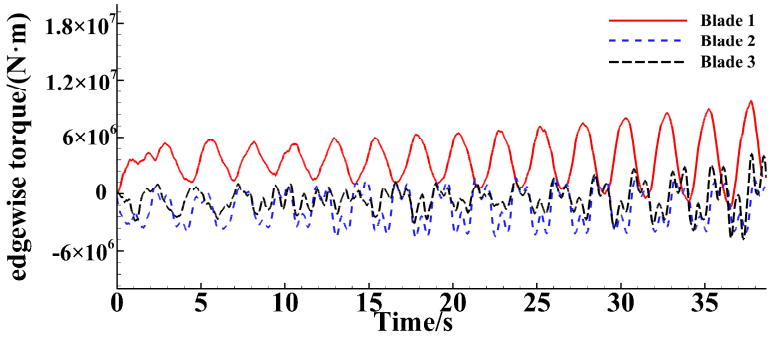

Figure 33. Time-domain plot of edgewise-direction moments at the root of three blades.

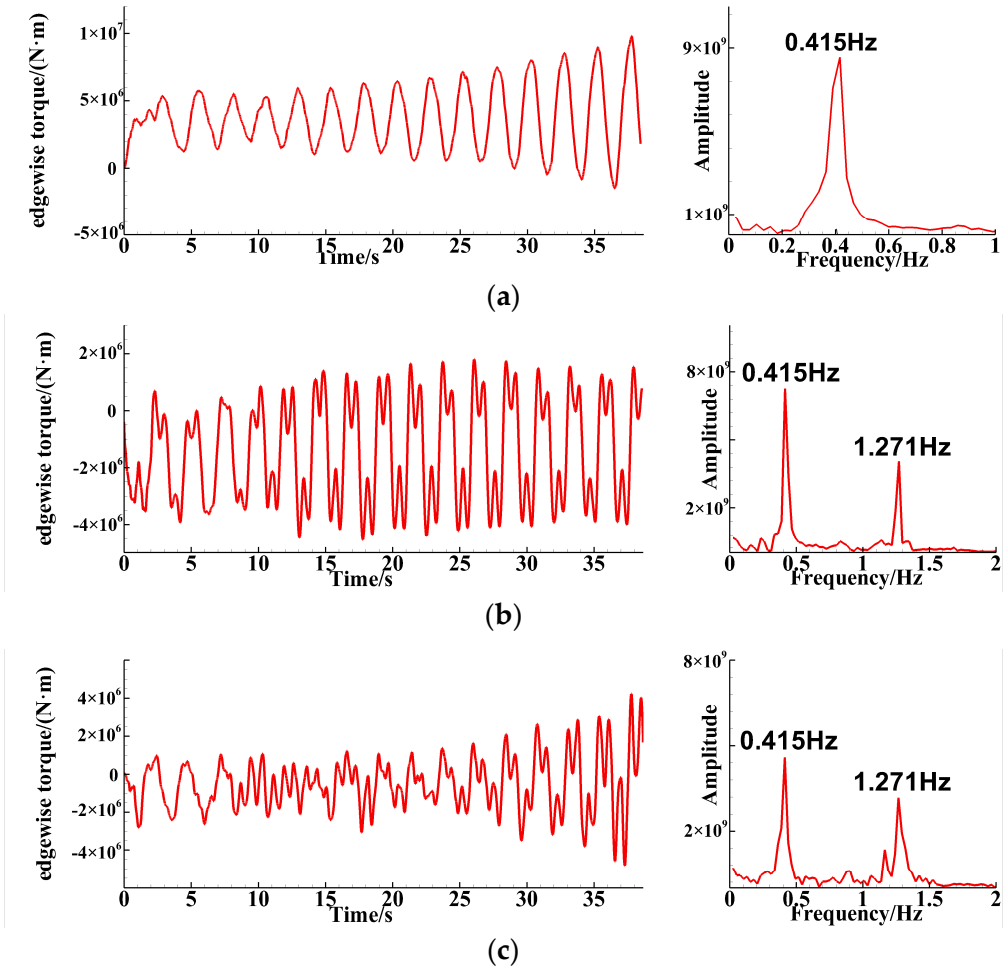

Figure 34. Time–frequency plot of the edgewise moment at the blade root. (**a**) blade 1; (**b**) blade 2; (**c**) blade 3.

Figure 35 delineates the bending moments at the root of the three blades in their respective flapwise directions. Based on Figure 35, it is evident that throughout the simulation, the flapwise moments of the three blades exhibit behavior similar to the flapwise deformation response at the blade tips. Figure 36a–c illustrate the flapwise-direction moment frequency plots for blade 1, blade 2 and blade 3, respectively. It can be observed that the flapwise moments for blade 1 and blade 2 tend to stabilize as the simulation progresses. Blade 1 exhibits an average flapwise moment of 15,000 kNm with an amplitude of approximately 1000 kNm, while blade 2 demonstrates an average flapwise moment of 23,000 kNm with an amplitude of around 2000 kNm. The frequency domain plot reveals a concurrent influence of both first-order and second-order flapwise modes on blade 1 and blade 2. The average

load of the flapping moment at the root of blade 3 is 6000 kNm, which is significantly smaller than the flapping moment at the root of blades 1 and 2. This may be due to the fact that blade 3 is oriented towards the ground in the downstream direction, while the incoming wind approaches the blade from the root towards the tip. Additionally, blade 3 is positioned in the wake region of blade 2, where small-scale disturbances in the inflow field may reduce the aerodynamic elastic response of blade 3.

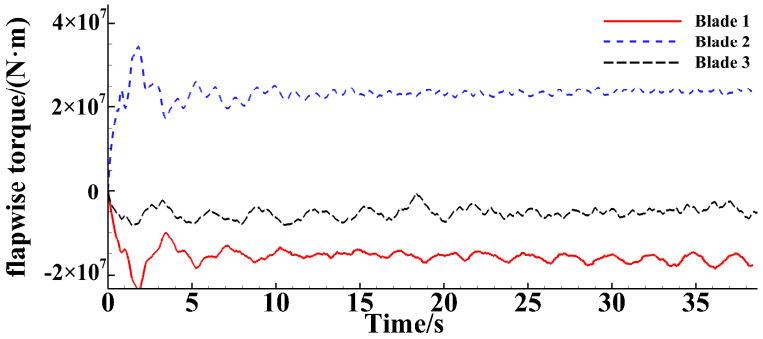

Figure 35. Time-domain plot of flapwise-direction moments at the root of three blades.

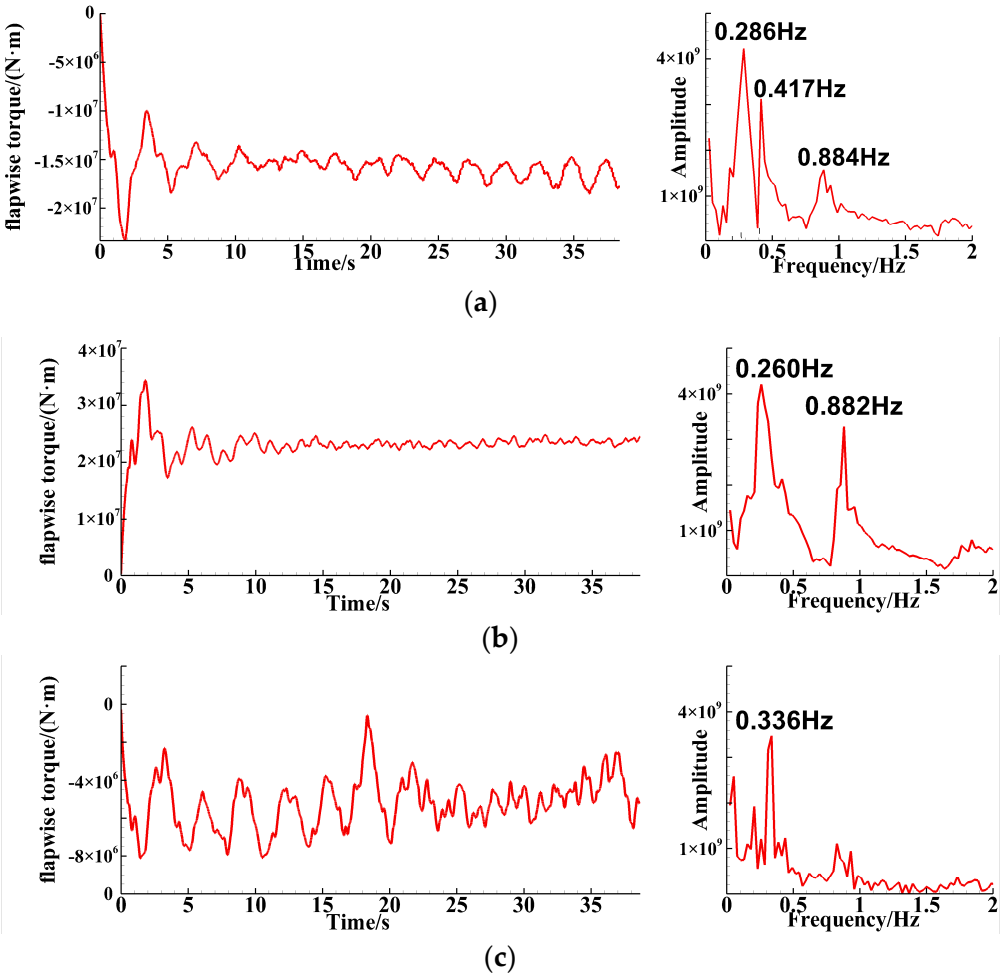

Figure 36. Time–frequency plot of the flapwise moment at the blade root. (**a**) blade 1; (**b**) blade 2; (**c**) blade 3.

5. Conclusions

This study develops a fluid–structure interaction framework based on computational fluid dynamics (CFD) and geometrically exact beam theory. By establishing data transfer methods between the flow solver and the structural solver, aerodynamic elastic simulations of a long flexible blade and a three-blade rotor model are successfully conducted. This study investigated the influence of gravity loading and turbulence intensity on the aeroelastic responses of individual blades and analyzed the differences in these responses caused by the rotor's three-blade configuration at different positions.

(1) Under gravity loading conditions, the vibration amplitude of the blade tip in the edgewise direction is significantly greater than that under unloaded conditions. Therefore, gravity cannot be overlooked in simulation and modeling. If the influence of gravity is disregarded during blade design, the aeroelastic response of the blade under actual operating conditions may exceed the design specifications, potentially resulting in accidents.

(2) Enhancing the turbulence intensity results in a reduction in both the magnitude and dominant frequency of deformation, force and moment in the edgewise direction at the blade root. This observation suggests that an increasing turbulence intensity contributes to the stability of the aeroelastic response. In practical scenarios, incoming flows frequently exhibit non-uniformity. Thus, during the design of the aerodynamic elasticity of wind turbine blades, opting for a uniform flow condition for stability can enhance the resilience of the blade aerodynamic elasticity.

(3) Under various operational conditions, the primary frequency of the vibration deformation response in the blade's edgewise direction consistently corresponds to the first-order edgewise mode frequency of the blade.

(4) Comparing the deformation responses in the convergence section of the blade's flapwise direction under different operating conditions with simultaneous gravity loading and varying turbulence intensities, it is indicated that under increased turbulence intensity, the inflow conditions lead to a transition of the vibration frequency from the first-order flapwise frequency to the first-order edgewise frequency. The time–frequency analyses of flapwise vibration for both single-blade and three-blade rotors indicate the coupling mechanism between the first flapwise mode and the first torsional mode of vibration. With increasing simulation time, the flapwise vibration will be primarily governed by the frequency of the first flapwise mode.

Author Contributions: Validation, P.L.; Writing—review & editing, X.W., R.L. and Y.L.; Supervision, C.G. and K.F. All authors have read and agreed to the published version of the manuscript.

Funding: This research received no external funding.

Data Availability Statement: The original contributions presented in the study are included in the article, further inquiries can be directed to the corresponding author.

Conflicts of Interest: Authors Yan Li and Pin Lv were employed by the company Beijing Goldwind Science & Creation Windpower Equipment Co., Ltd. The remaining authors declare that the research was conducted in the absence of any commercial or financial relationships that could be construed as a potential conflict of interest.

References

1. Dose, B.; Rahimi, H.; Herráez, I.; Stoevesandt, B.; Peinke, J. Fluid-structure coupled computations of the NREL 5 MW wind turbine blade during standstill. *J. Phys. Conf. Ser.* **2016**, *753*, 022034. [CrossRef]
2. Hansen, M.H. Aeroelastic instability problems for wind turbines. *Wind Energy* **2007**, *10*, 551–577. [CrossRef]
3. Heinz, J.C.; Sørensen, N.N.; Zahle, F.; Skrzypiński, W. Vortex-induced vibrations on a modern wind turbine blade. *Wind Energy* **2016**, *19*, 2041–2051. [CrossRef]
4. Hansen, M.H. Aeroelastic stability analysis of wind turbines using an eigenvalue approach. *Wind Energy* **2004**, *7*, 133–143. [CrossRef]
5. Razak, N.A.; Andrianne, T.; Dimitriadis, G. Flutter and stall flutter of a rectangular wing in a wind tunnel. *AIAA J.* **2011**, *49*, 2258–2271. [CrossRef]

6. Shitang, K.E.; Manman, L.U.; Hongxin, W.U.; Muen, G.A.; Wenxin, T.I.; Hao, W.A.; Shuo, W.A. Experimental study on the post-flutter morphological chracteristics and energy dissipation of a 15 MW wind turbine blade. *Acta Aerodyn. Sin.* **2022**, *40*, 169–180.
7. Lu, M.M.; Ke, S.T.; Wu, H.X.; Gao, M.E.; Tian, W.X.; Wang, H. Blade root reaction method for predicting flutter critical wind speed of 15 MW ultra-long flexible blades based on aeroelastic tests. *J. Vib. Eng.* **2023**, *36*, 718–728.
8. Liu, X.; Ma, X.-w.; Shen, S.; Chen, Y. Analysis of the influence of vibration and deformation of the blade on the aerodynamic damping. *Acta Aerodyn. Sin.* **2013**, *31*, 407–412.
9. Yan, C.; Linwei, Z.; Xiong, L.; Qiong, L. Response analysis of aeroelasticity for hawt flexible blade. *Acta Energiae Solaris Sin.* **2014**, *35*, 74–82.
10. Yang, B. Research on Fluid-Structure Coupling of Horizontal Axis Wind Turbine Blades Based on FAST. Master's Thesis, North China Electric Power University, Baoding, China, 2020.
11. Chen, A.-J.; Wang, C.; Jia, Y.-Y.; Liu, Q.-K. Computation and analysis of aerodynamic performance of wind turbine blade based on BEM. *Eng. Mech.* **2021**, *38*, 264–268.
12. Skrzypiński, W.R.; Gaunaa, M.; Sørensen, N.; Zahle, F.; Heinz, J. Self-induced vibrations of a DU96-W-180 airfoil in stall. *Wind Energy* **2014**, *17*, 641–655. [CrossRef]
13. Skrzypiński, W.; Gaunaa, M.; Sørensen, N.; Zahle, F.; Heinz, J. Vortex-induced vibrations of a DU96-W-180 airfoil at 90° angle of attack. *Wind Energy* **2014**, *17*, 1495–1514. [CrossRef]
14. Heinz, J.C.; Sørensen, N.N.; Zahle, F. Fluid–structure interaction computations for geometrically resolved rotor simulations using CFD. *Wind Energy* **2016**, *19*, 2205–2221. [CrossRef]
15. Dose, B.; Rahimi, H.; Herráez, I.; Stoevesandt, B.; Peinke, J. Fluid-structure coupled computations of the NREL 5 MW wind turbine by means of CFD. *Renew. Energy* **2018**, *129*, 591–605. [CrossRef]
16. Lu, P. Research on Rotating Blade Solid Coupling of Large Horizontal Axis Wind Turbine. Ph.D. Thesis, Northwestern Polytechnical University, Xi'an, China, 2016.
17. Leng, J.; Gao, Z.; Zheng, X.; Li, Y. Aeroelastic analysis of a 5 MW offshore wind turbine based on actuator line method. *Acta Aerodyn. Sin.* **2022**, *40*, 203–209.
18. Savino, A.; Cocco, A.; Zanotti, A.; Tugnoli, M.; Masarati, P.; Muscarello, V. Coupling Mid-Fidelity Aerodynamics and Multibody Dynamics for the Aeroelastic Analysis of Rotary-Wing Vehicles. *Energies* **2021**, *14*, 6979. [CrossRef]
19. Cocco, A.; Mazzetti, S.; Masarati, P.; van't Hoff, S.; Timmerman, B. Numerical Whirl–Flutter analysis of a tiltrotor semi-span wind tunnel model. *CEAS Aeronaut. J.* **2022**, *13*, 923–938. [CrossRef]
20. Leng, J.; Gao, Z.; Wu MC, H.; Guo, T.; Li, Y. A fluid–structure interaction model for large wind turbines based on flexible multibody dynamics and actuator line method. *J. Fluids Struct.* **2023**, *118*, 103857. [CrossRef]
21. Reissner, E. On one-dimensional large-displacement finite-strain beam theory. *Stud. Appl. Math.* **1973**, *52*, 87–95. [CrossRef]
22. Wang, Q.; Sprague, M.A.; Jonkman, J.; Johnson, N.; Jonkman, B. BeamDyn: A high-fidelity wind turbine blade solver in the FAST modular framework. *Wind Energy* **2017**, *20*, 1439–1462. [CrossRef]
23. Hodges, D.H. Geometrically exact, intrinsic theory for dynamics of curved and twisted anisotropic beams. *AIAA J.* **2003**, *41*, 1131–1137. [CrossRef]
24. Hsu, M.C.; Akkerman, I.; Bazilevs, Y. Finite element simulation of wind turbine aerodynamics: Validation study using NREL Phase VI experiment. *Wind Energy* **2014**, *17*, 461–481. [CrossRef]
25. Jensen, F.M.; Arconada, J.O.; Werk, M.; Berggreen, C.; Sørensen, J.D.; Zhong, G.; Haans, W. Torsional Effects on Wind Turbine Blades and Impact on Field Damages. *IOP Conf. Ser. Mater. Sci. Eng.* **2023**, *1293*, 012005. [CrossRef]
26. Qiao, X.H.; Gao, Z.T.; Wang, T.G.; Wang, L.; Ke, S.T. Nonlinear aeroelastic response analysis of 100-meter-scale flexible wind turbine blades. *Acta Aerodyn. Sin.* **2022**, *40*, 220–230.
27. Rmsay, R.F.; Hoffman, M.J.; Gregorek, G.M. *Effects of Grit Roughness and Pitch Oscillations on the S810 Airfoil*; National Renewable Energy Lab. (NREL): Golden, CO, USA, 1996.
28. Janiszewska, J.M.; Ramsay, R.R.; Hoffmann, M.J.; Gregorek, G.M. *Effects of Grit Roughness and Pitch Oscillations on the S814 Airfoil*; National Renewable Energy Lab. (NREL): Golden, CO, USA, 1996.
29. Couturier, P.J.; Skjoldan, P.F. Implementation of an advanced beam model in BHawC. *J. Phys. Conf. Ser.* **2018**, *1037*, 062015. [CrossRef]
30. Hansen, M.H. Anisotropic damping of Timoshenko beam elements. (Denmark. Forskningscenter Risoe. Risoe-R; No. 1267). 2001. Available online: https://orbit.dtu.dk/en/publications/anisotropic-damping-of-timoshenko-beam-elements (accessed on 4 July 2024).
31. Bazoune, Y.A.K. Shape functions of three-dimensional timoshenko beam element. *J. Sound Vib.* **2003**, *259*, 473–480. [CrossRef]
32. Pradhan, S.; Modi, V.J.; Misra, A.K. Order N Formulation for Flexible Multibody Systems in Tree Topology: Lagrangian Approach. *J. Guid. Control. Dyn.* **1997**, *20*, 665672. [CrossRef]
33. Torby, B.J.; Kimura, I. Dynamic Modeling of a Flexible Manipulator with Prismatic Links. *J. Dyn. Syst. Meas. Control.* **1999**, *121*, 691696. [CrossRef]
34. Bir, G. Multi-blade coordinate transformation and its application to wind turbine analysis. In Proceedings of the 46th AIAA/ASME Wind Energy Symposium, Reno, NV, USA, 7–10 January 2008; pp. 82–86.
35. Stewart, G.W. A Krylov–Schur Algorithm for Large Eigenproblems. *SIAM J. Matrix Anal. Appl.* **2001**, *23*, 601–614. [CrossRef]

36. Wu, X.; Feng, K.; Li, Q. A Numerical Method for the Dynamics Analysis of Blade Fracture Faults in Wind Turbines Using Geometrically Exact Beam Theory and Its Validation. *Energies* **2024**, *17*, 824. [CrossRef]
37. Guodong, R.; Wenlei, S.; Xiuling, R. Fatigue research on vane of wind power generator based on cosimulation. *Mach. Tool Hydraul* **2010**, *38*, 100–102.
38. Lü, P.; Liao, M.; Xu, Y.; Yin, Y. Beam Finite Element for Wind Turbine Bladebased on Geometrically Exact Beam Theory. *Acta Energiae Solaris Sin* **2015**, *36*, 2422–2428.